The Astrophysical Journal Letters, 979:L47 (12pp), 2025 February 1 https://doi.org/10.3847/2041-8213/ada7f8

X-Ray Dips and Polarization Angle Swings in GX 13+1

Alessandro Di Marco[1], Fabio La Monaca[1,2], Anna Bobrikova[3], Luigi Stella[4], Alessandro Papitto[4], Juri Poutanen[3], Maria Cristina Baglio[5], Matteo Bachetti[6], Vladislav Loktev[3], Maura Pilia[6], and Daniele Rogantini[7]
[1] INAF Istituto di Astrofisica e Planetologia Spaziali, Via del Fosso del Cavaliere 100, 00133 Roma, Italy; alessandro.dimarco@inaf.it
[2] Dipartimento di Fisica, Università degli Studi di Roma "Tor Vergata," Via della Ricerca Scientifica 1, 00133 Rome, Italy
[3] Department of Physics and Astronomy, 20014, University of Turku, Finland
[4] INAF Osservatorio Astronomico di Roma, Via Frascati 33, 00078 Monte Porzio Catone (RM), Italy
[5] INAF Osservatorio Astronomico di Brera, Via Bianchi 46, I-23807 Merate (LC), Italy
[6] INAF Osservatorio Astronomico di Cagliari, Via della Scienza 5, 09047 Selargius (CA), Italy
[7] Department of Astronomy and Astrophysics, University of Chicago, Chicago, IL 60637, USA
Received 2024 September 14; revised 2024 December 23; accepted 2025 January 4; published 2025 January 31

Abstract

We present the result from the 2024 April observation of the low-mass X-ray binary GX 13+1 with the Imaging X-ray Polarimetry Explorer (IXPE), together with Neutron Star Interior Composition Explorer and Swift- X-Ray Telescope coordinated observations. Two light-curve dips were observed; during them, the harder Comptonized spectral component was dominant and the polarization degree (PD) higher than in the softer, off-dip intervals. Through a joint analysis of the three IXPE observations, which also included the dip from the first observation, we demonstrate that the polarization properties varied in response to the intensity and spectral hardness changes associated with the dips. The PD attained values up to ∼4%. The polarization angle (PA) showed a swing of ∼70° across the dip and off-dip states, comparable to the continuous rotation seen during the first IXPE observation. We discuss these results in the context of models for polarized emission from the accretion disk and the boundary/spreading layer on the neutron star surface. We also draw attention to the role that an extended accretion disk corona or disk wind can play in generating high PDs and, possibly, swings of the PA.

Unified Astronomy Thesaurus concepts: Stellar accretion disks (1579); Neutron stars (1108); Polarimetry (1278); Spectropolarimetry (1973); Low-mass x-ray binary stars (939)

1. Introduction

Low-mass X-ray binaries (LMXBs) are systems in which a compact object accretes matter from a low-mass companion star via Roche-lobe overflow and a disk. Systems hosting a weakly magnetized neutron star (WMNS) comprise two main classes, named Z and Atoll sources, after the characteristic shape they trace in the X-ray color–color diagram (CCD). Z sources are persistent and bright, displaying luminosities close to the Eddington limit, whereas Atoll sources are about 1 decade less luminous, frequently display thermonuclear bursting activity, and in some cases undergo transient outbursts; see, e.g., M. van der Klis (1989). The millisecond spin periods that are expected to characterize WMNSs in LMXBs have been detected only from a few dozen Atoll sources through coherent pulsations during transient outbursts and/or burst oscillations during thermonuclear bursts (A. Papitto et al. 2014). Fast aperiodic and quasiperiodic variability is detected in the range between few Hz and ∼1 kHz and presents clear similarities in both Z and Atoll sources. The energy spectra of accreting WMNSs can be described by a model consisting of a multicolor blackbody, representing the thermal emissions from the inner accretion disk regions, and a higher-energy Comptonized continuum, which dominates the spectrum and likely originates from the boundary layer (BL; N. I. Shakura & R. A. Sunyaev 1988; R. Popham & R. Sunyaev 2001) between the disk and the neutron star (NS) or the plasma layer at the NS surface, the so-called spreading layer (SL; N. A. Inogamov & R. A. Sunyaev 1999; V. Suleimanov & J. Poutanen 2006). Reflection spectrum (T. R. White et al. 1988; A. C. Fabian et al. 1989; I. M. George & A. C. Fabian 1991; L. Giridharan et al. 2023; R. M. Ludlam 2024) caused by radiation intercepted and reprocessed by the accretion disk is also observed in many cases. The presence of powerful outflows, in the form of collimated fast jets emitted perpendicularly to the disk (M. C. Baglio et al. 2017) and/or fan-shaped slower winds launched from moderate altitudes above the disk (J. L. Allen et al. 2018), have also been established in a number of black hole and NS LMXBs.

X-ray flux modulations at the orbital period are sometimes present, especially in higher-inclination (>60°) systems. In most cases, the modulation consists of intensity dips arising from obscuration due to increased photoelectric absorption, repeated once (or twice) per orbit, which are variable in shape and present some jitter in the orbital phase. These dips are likely due to clumps in the outermost disk region, close to the point where the accretion stream from the companion impacts. X-ray eclipses resulting from direct occultation of the emitting regions by the companion star are rare phenomena. Residual X-ray flux is observed at the bottom of eclipses (e.g., in EXO 0748−676). This, together with the smooth, often low-amplitude, orbital modulation observed in some systems, tests that some plasma extends well above the disk midplane and scatters radiation along our line of sight (for a review, see, e.g., A. N. Parmar & N. E. White 1988). This region is referred to as the extended accretion disk corona (hereafter ADC or extended disk atmosphere; see, e.g., I. Psaradaki et al. 2018); it is expected to be optically thin in X-rays and populated by highly ionized matter. X-ray spectroscopic studies of selected high-inclination WMNSs have confirmed the existence of such an extended ADC in EXO 0748−676 (M. A. Jimenez-Garate et al. 2003), 4U 1822−37 (J. Cottam et al. 2001), or 2S 0921−63 (T. R. Kallman et al. 2003). The nature and geometry of ADCs

are not well understood, but different models predict their existence (N. E. White & S. S. Holt 1982; K. A. Miller & J. M. Stone 2000).

X-ray polarimetry has introduced a novel diagnostic for NS LMXBs through two new observables—the polarization angle (PA) and the polarization degree (PD)—and their variability. This new information can provide insight into the accretion physics of these objects and the geometry of the BL (and/or SL) and possibly of the ADC and the disk wind. Imaging X-ray Polarimetry Explorer (IXPE) has already observed several systems. For Cyg X-2, the PA was aligned along the position angle of the radio jet (R. Farinelli et al. 2023), which is likely perpendicular to the accretion disk. On the other hand, F. La Monaca et al. (2024) observed a significant difference between the PA measured from Sco X-1 and the jet position angle, suggesting a more complex geometry for this source. In Cir X-1 (J. Rankin et al. 2024), XTE J1701−462 (M. Cocchi et al. 2023), and GX 5−1 (S. Fabiani et al. 2024), the polarization varied with the state and/or the hardness of the source, with a PA rotation up to 67° in Cir X-1 and PD passing from ∼4% in the horizontal branch to ∼1% in the normal/flaring branches of Z sources (A. Di Marco & IXPE Science Team 2024). In the Atoll sources GX 9+9 (F. Ursini et al. 2023), 4U 1820−303 (A. Di Marco et al. 2023a), and 4U 1624−49 (M. L. Saade et al. 2024), and the Z source GX 340+0 (Fabio La Monaca et al. 2024), a dependence of the PD on energy was observed.

GX 13+1 is a persistent LMXB located at a distance of 7 ± 1 kpc (R. M. Bandyopadhyay et al. 1999). J. R. Fleischman (1985) observed for the first time Type I X-ray bursts in this system, allowing unambiguous identification of its compact object as an NS. It has been classified as a bright Atoll source (G. Hasinger & M. van der Klis 1989) or a Z source based on the strong secular evolution of its CCD and hardness–intensity diagrams (HIDs) that showed peculiar features (L. Giridharan et al. 2023). For example, in L. Stella et al. (1985), the source HID shows two crossing branches, while R. S. Schnerr et al. (2003) reported a shape similar to Atoll sources but with a pattern opposite to the usual one observed in other WMNSs. Moreover, its fast variability properties, including an individual quasiperiodic oscillation at ∼61 Hz, are not easily classified (J. Homan et al. 1998). In general, identifying the source state(s) was found to be more difficult for GX 13+1 than for other LMXBs.

GX 13+1 belongs to the group of dipping sources (M. Diaz Trigo et al. 2009; R. D'Aì et al. 2014; R. Iaria et al. 2014). Its dips are reported to occur periodically every 24.5274(2) days (R. Iaria et al. 2014) and are used to define the zero phase. The dip periodicity is compatible with the orbital period of the source reported by R. H. D. Corbet et al. (2010) on the basis of the modulation of the *K* band and X-ray light curves. Off-phase X-ray dips were also occasionally observed (M. Diaz Trigo et al. 2012; A. Bobrikova et al. 2024b).

Spectral analyses of GX 13+1 have been performed in the past based on data collected with different satellites (see, e.g., E. A. Saavedra et al. 2023 and references therein). In particular, the XMM-Newton observations analyzed by M. Diaz Trigo et al. (2012) showed a pronounced obscuration along the line of sight. This is consistent with the presence of a disk wind and/or a warm disk atmosphere, provided the inclination of the system is in the 60°–80° range. Further analysis of the same XMM-Newton data by T. Maiolino et al. (2019) indicated an inclination ∼60°, whereas a ∼70° value was obtained from the NuSTAR data by E. A. Saavedra et al. (2023).

IXPE conducted two observations of GX 13+1 before the one presented in this Letter—the first on 2023 October 17–19 (A. Bobrikova et al. 2024b) and the second on 2024 February 25–27 (A. Bobrikova et al. 2024a). In the first IXPE observation, about 1 week before the periodic dip (orbital phase 0.74–0.83), GX 13+1 exhibited peculiar characteristics. The source showed a continuous rotation of the PA by ∼70° together with a change in the dependence of PD on energy before and after a dip (A. Bobrikova et al. 2024b). Correspondingly, the spectral properties showed little to no change. The second observation of GX 13+1 was carried out simultaneously by IXPE and Swift X-Ray Telescope (XRT) shortly after the end of the periodic dip (orbital phase 0.08–0.16). Polarization was measured with an almost constant PD of ∼2.5% and PA of ∼24° (A. Bobrikova et al. 2024a). The Swift-XRT spectrum of the source remained nearly constant during the IXPE observation. A. Bobrikova et al. (2024a) studied the differences and similarities between these two observations; the primary finding was that the second observation displayed a notably higher overall polarization, despite the almost identical state of the source.

The present Letter is based on IXPE and coordinated observations of GX 13+1 that were carried out in 2024 April. Observations and data reduction are presented in Section 2 and the polarimetric and spectral analyses in Section 3. We discuss our results in Section 4 and present conclusions in Section 5.

2. Observations and Data Reduction

The IXPE payload consists of three identical telescopes, providing imaging and spectral polarimetry over the 2–8 keV energy band (P. Soffitta et al. 2021; M. C. Weisskopf et al. 2022). It observed GX 13+1 for the third time (Observation ID 03003401) in the period 2024 April 20 20:49–April 23 01:01 UTC (orbital phase 0.33–0.42) for a total effective exposure time of ∼100 ks for each telescope (see Table 1). The 2–8 keV IXPE light curve binned every 200 s is shown in Figure 1, along with the hardness ratio of the rates in the 2–4 and 4–8 keV bands.

Two coordinated pointings, covering the 0.2–10 keV energy range, were carried out with Swift-XRT (N. Gehrels et al. 2004) to gather additional spectral information (see Table 1). The second pointing consisted of three different snapshots. All Swift-XRT observations were performed in Windowed Timing mode (WT). The Neutron Star Interior Composition Explorer (NICER) on board the International Space Station also pointed GX 13+1 with its concentrator X-ray optics and silicon drift detectors operating in the 0.7–12 keV energy range (K. C. Gendreau et al. 2016). GX 13+1 observations were collected in three Observation IDs (see Table 1).[8]

IXPE data were processed for polarimetric analysis using the IXPEOBSSIM package version 31.0.1 (L. Baldini et al. 2022). For spectral and spectropolarimetric analysis, data extraction was performed using HEASOFT version 6.33.2 and the standard FTOOLS. In the case of IXPE, we used the CALDB released on 2024 February 28. Source events were extracted from IXPE data by selecting a circular region of radius 100″ centered on the position of the source, using SAOIMAGEDS9.[9] Due to the high flux of the source, the background

[8] Observation ID 7701010101 covered only a very short interval of the IXPE observation, so in the following spectral analysis we only considered the other two Observation IDs.

[9] https://sites.google.com/cfa.harvard.edu/saoimageds9

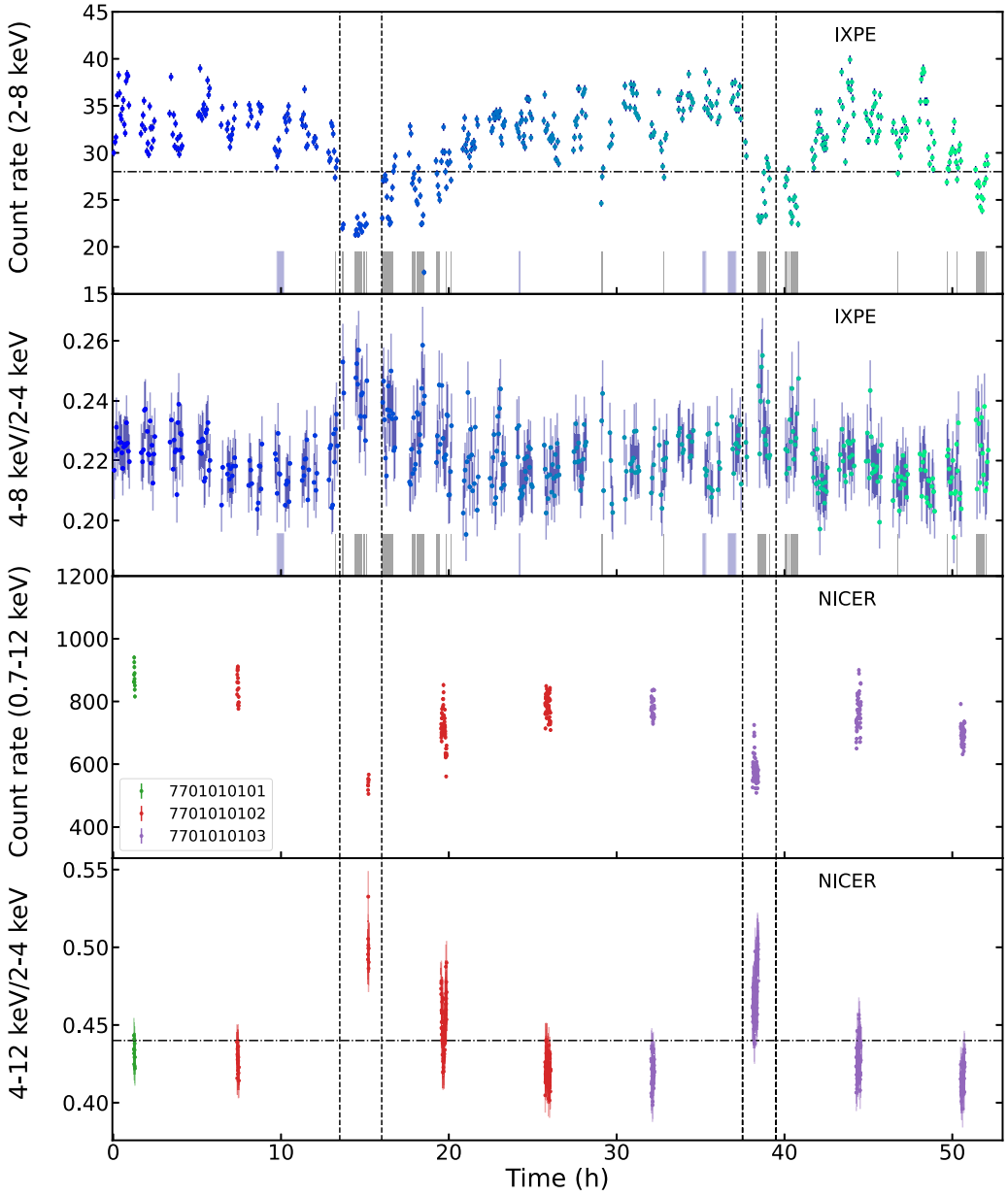

Figure 1. From top to bottom: light curve of the third IXPE observation of GX 13+1 obtained in the 2–8 keV combining the three telescopes binned in 200 s and the corresponding hardness ratio as a function of time with the same binning; NICER 20 s binned light curve in the 0.7–12 keV band, normalized to 50 detectors, and the corresponding hardness ratio as a function of time. In the first two panels the light-blue shaded bars mark the Swift-XRT observation periods, and the black horizontal dashed–dotted line reports the threshold applied to select the dip state periods (corresponding to the gray vertical shaded bars) in the spectropolarimetric analysis (count rate <28 counts s^{-1}) with respect to off-dip (count rate $\geqslant 28$ counts s^{-1}). The vertical black dashed lines reported in these panels show the periods we applied to select the dips in the `pcube` model-independent analysis. In the fourth panel, the horizontal dashed–dotted black line marks the threshold separating the dip time intervals (hardness ratio >0.44) from the off-dip intervals (hardness ratio $\leqslant 0.44$) in the NICER data.

Table 1
Coordinated X-Ray Campaign during the Third IXPE Observation of GX 13+1

	Obs ID	Start (UTC)	Stop (UTC)	Telescope	Exp. Time (ks)
IXPE	03003401	2024 Apr 20 20:49	2024 Apr 23 01:01	DU 1	99.9
...	...	...	...	DU 2	100.0
...	...	...	...	DU 3	100.1
Swift-XRT	00036688052	2024 Apr 21 06:35	2024 Apr 21 06:58	XRT-WT	1.4
...	00036688053	2024 Apr 21 21:01	2024 Apr 22 09:55	XRT-WT	2.4
NICER	7701010101	2024 Apr 20 04:54	2024 Apr 20 22:06	⋯	2.5
...	7701010102	2024 Apr 21 04:08	2024 Apr 21 22:52	⋯	3.0
...	7701010103	2024 Apr 22 04:41	2024 Apr 22 23:33	⋯	3.9

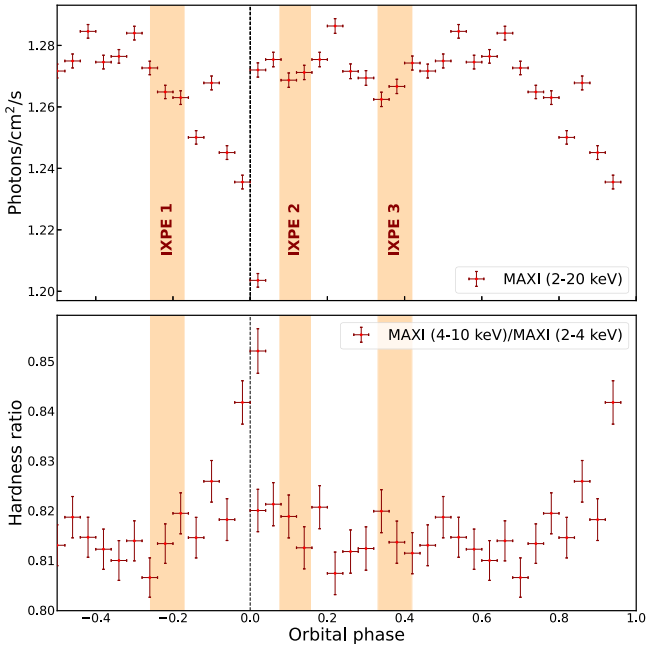

Figure 2. MAXI folded light curve and hardness ratio of GX 13+1 using the ephemeris of R. Iaria et al. (2014). The periodic dip defines zero phase. The orbital phase intervals covered in the three IXPE observations (IXPE 1, 2, 3) are marked with vertical orange strips. It is apparent that the spectral hardness increases when the source count rate decreases.

was not subtracted, as prescribed by A. Di Marco et al. (2023b). In the model-independent polarimetric analysis, based on the `pcube` algorithm in IXPEOBSSIM, the unweighted analysis was adopted, whereas for the model-dependent spectral and spectropolarimetric analyses we used the "weighted analysis." The latter is based on the ellipticity of the photoelectrons tracks collected by the IXPE Detector Units (DUs) and follows the approach of A. Di Marco et al. (2022). Data were binned so as to have at least 30 counts per energy channel in the spectral analysis, while in the spectropolarimetric analysis we applied a constant energy binning of 120 eV for all three energy distributions of the Stokes parameters I, Q, and U, given the lower statistic available in the Q and U spectra.

The extraction of source and background events was performed in the Swift-XRT data with SAOIMAGEDS9 using an annulus (inner radius of about 5″ and an outer radius of about 40″) in order to avoid possible pileup effects (P. Romano et al. 2006); the source annulus was centered at the GX 13+1 coordinates, and the background annulus about 80″ off-source. The Swift-XRT data were fitted in the 0.8–8 keV band to optimize the statistics and grouped so as to have at least 30 counts per bin. The response matrices released in the HEASARC CALDB on 2023 July 25 were applied in the analysis.

NICER data were processed with the NICER Data Analysis Software v012a released on 2024 February 9 and with the CALDB version released on 2024 February 27. The background spectra were estimated by applying the SCORPEON model. All spectra, fitted in the 1.5–10 keV energy band, were grouped so as to have at least 30 counts per bin. Light curves, HID, and time selections were obtained using STINGRAY (D. Huppenkothen et al. 2019a, 2019b; M. Bachetti et al. 2024).

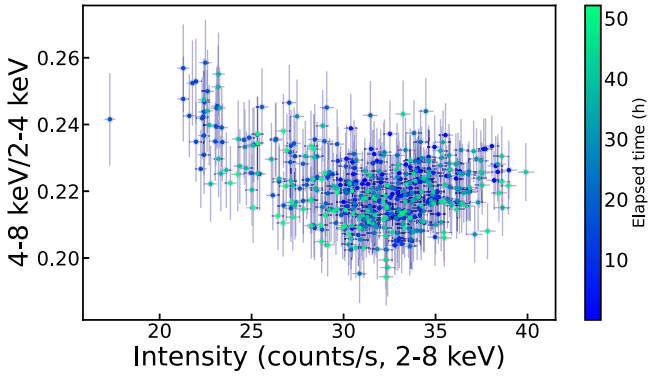

Figure 3. HID obtained from IXPE data, using the same energy bands (4–8 keV and 2–4 keV) and the same binning (200 s) as in A. Bobrikova et al. (2024a, 2024b). The colors follow the same time behavior as in Figure 1, and the color bar is on the right.

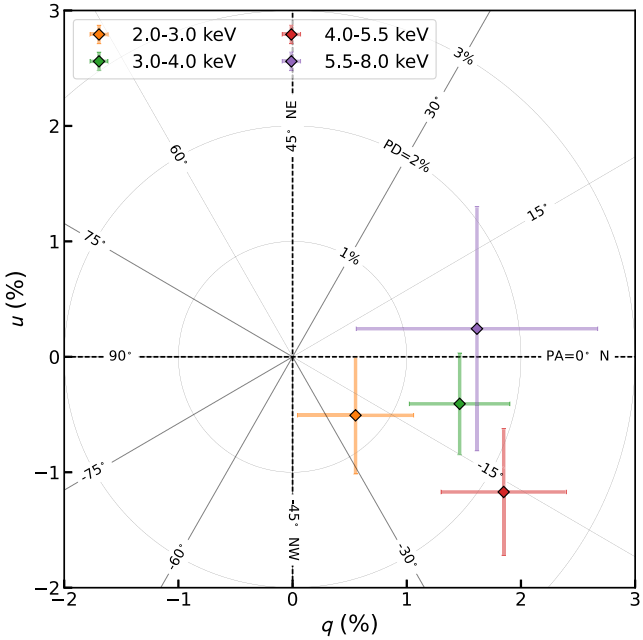

Figure 4. Normalized Stokes parameters $q = Q/I$ and $u = U/I$ in different energy bins as obtained by `pcube` in IXPEOBSSIM. The error bars are at 68% CL. No significant trend of the polarization with energy is observed.

3. Data Analysis

The IXPE light curve of the third observation of GX 13+1 displayed two erratic, nonperiodic dips, during which the source count rate decreased by 20%–30% and the hardness ratio increased (see Figure 1). The first lasted about 12 ks (including ingress, dip phase, and egress), the second ∼5 ks. Both dips showed fast continuous ingress, while the egress was characterized by marked variability. Their orbital phase was 0.334 and 0.395, thus away from the periodic dip that defines the zero phase (see Figure 2, which also displays the orbital phase intervals covered by the other IXPE observations).

The HID obtained from the IXPE data is shown in Figure 3. NICER data partially covered the two dips, as shown in Figure 1, thus making detailed spectral modeling possible. No Swift-XRT data were taken during the dips.

3.1. Polarimetric Analysis

IXPE data in the 2–8 keV band were used in the polarimetric analysis. We obtained an average polarization of PD = 1.4% ± 0.3%

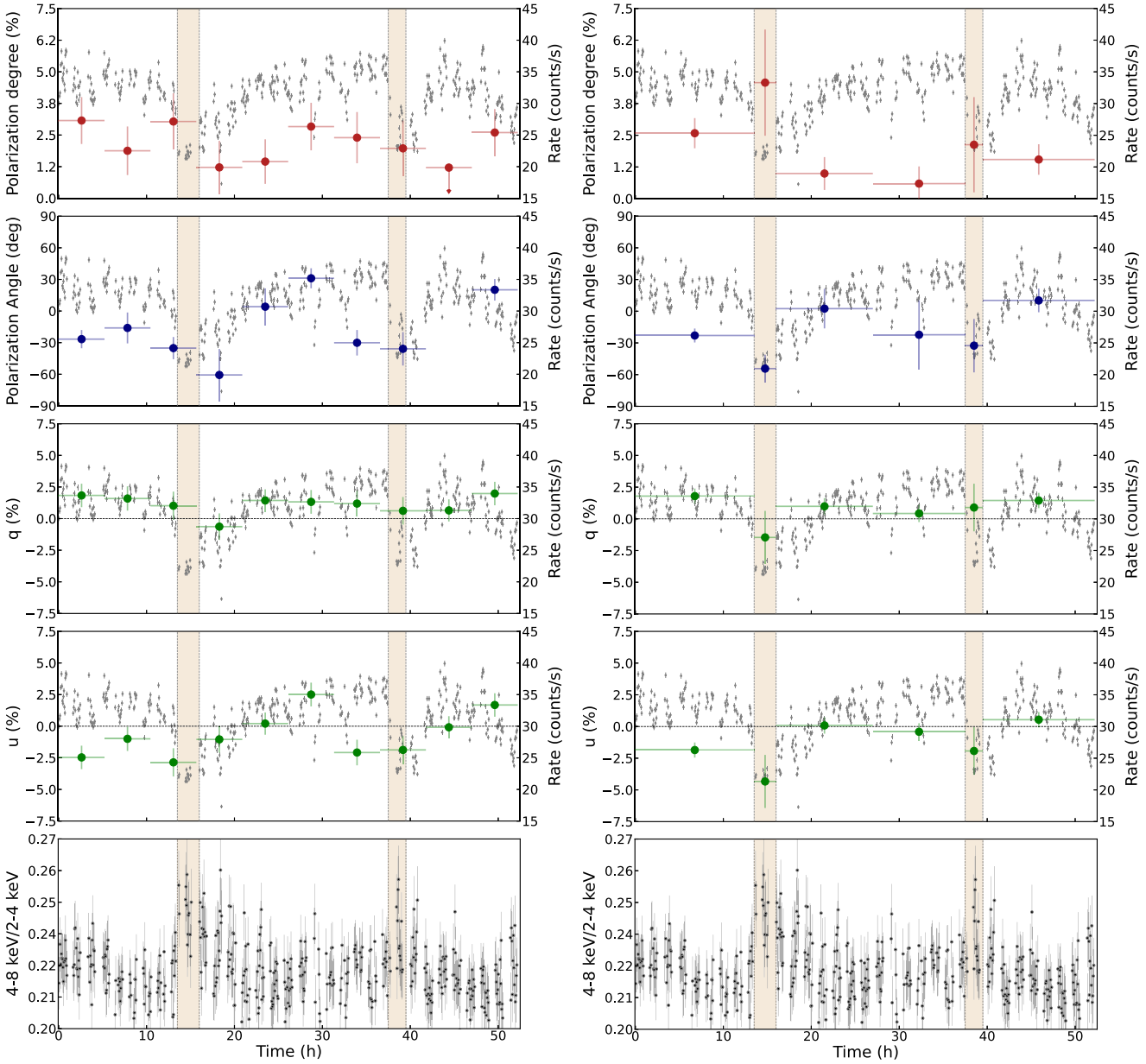

Figure 5. Polarization properties of GX 13+1 as a function of time during the third IXPE observation. The panels from top to bottom show PD, PA, $q = Q/I$, $u = U/I$, and the hardness ratio along the observation. The gray points in the top four panels show the 2–8 keV count rate (right axis). Left panels: a constant binning of ∼5.2 hr is adopted. Right panels: the observation is divided into six time bins, two of them corresponding to the dips, and the other four covering intervals before, after, and between the two dips. Errors are at 68% CL.

Table 2
Best-fit Parameters for the Spectral Model `tbabs*(diskbb+bbodyrad)` as Obtained from the Two Swift-XRT Spectra in the 0.8–8.0 keV Energy Band

ObsID	`tbabs`	`diskbb`		`bbodyrad`		χ^2/d.o.f.	$\text{Flux}_{2-8\ \text{keV}}$	Hardness
	$N_{\rm H}$ (10^{22} cm^{-2})	$kT_{\rm in}$[a] (keV)	Norm	$kT_{\rm bb}$ (keV)	Norm		(10^{-9} erg s^{-1} cm^{-2})	
00036688052	4.63 ± 0.10	[1.0]	370 ± 20	$1.38^{+0.04}_{-0.03}$	150 ± 20	610/568	6.0	0.30
00036688053	4.60 ± 0.07	[1.0]	360 ± 20	1.46 ± 0.02	160 ± 12	660/638	6.8	0.35

Notes. Errors are reported at 68% CL.
[a] Fixed.

with the PA of $-11° \pm 7°$ (hereafter errors are at 68% confidence level, CL, unless stated otherwise). A search for energy trends in the polarization was carried out. The results, shown in Figure 4, are compatible with an energy-independent polarization to within 2σ.

We investigated polarization properties on timescales shorter than the observation duration by using ∼5.2 hr-long intervals. The results in Figure 5 left show a marked variability in the PA, which evolves in time in a noncontinuous way. We note that during the first IXPE observation of GX 13+1 the PA

Table 3
Best-fit Parameters for the Spectral Model tbabs*cabs*warmabs*(diskbb+bbodyrad+Gauss) as Obtained from Different NICER Spectra in the 1.5–10.0 keV Energy Band

Observation ID		7701010102		7701010103	
State		Dip	Off-dip	Dip	Off-dip
tbabs	$N_{\rm H}$ (10^{22} cm^{-2})	$3.75^{+0.10}_{-0.02}$	$3.61^{+0.07}_{-0.01}$	$3.69^{+0.01}_{-0.02}$	$3.58^{+0.07}_{-0.01}$
cabs[a]	$N_{\rm H}$ (10^{22} cm^{-2})	[61]	[48]	[40]	[47]
warmabs[b]	$N_{\rm H}$ (10^{22} cm^{-2})	51^{+3}_{-2}	40^{+2}_{-1}	33 ± 2	39 ± 2
...	$r \log \xi$	$3.58^{+0.01}_{-0.06}$	$3.52^{+0.05}_{-0.02}$	$3.53^{+0.08}_{-0.02}$	$3.50^{+0.01}_{-0.02}$
...	$v_{\rm turb}$ (km s^{-1})	117^{+40}_{-13}	271^{+26}_{-4}	210 ± 40	274^{+30}_{-7}
...	velocity (km s^{-1})	− 2410 ± 30	− 2332 ± 15	-1951^{+7}_{-20}	− 1962 ± 15
diskbb	$kT_{\rm in}$ (keV)	0.52 ± 0.14	1.02 ± 0.06	0.52 ± 0.03	1.09 ± 0.01
	norm	2450^{+50}_{-30}	237 ± 2	1726^{+30}_{-20}	174^{+690}_{-2}
	$R^{c}_{\rm in}$ (km)	$59.2^{+1.2}_{-0.7}$	$18.4^{+0.9}_{-0.2}$	$49.7^{+0.9}_{-0.6}$	$15.8^{+63.8}_{-0.2}$
bbodyrad	$kT_{\rm bb}$ (keV)	1.08 ± 0.07	1.20 ± 0.06	1.11 ± 0.02	1.17 ± 0.02
...	norm	773^{+3}_{-50}	432 ± 2	498^{+43}_{-2}	420^{+40}_{-2}
...	$R^{c}_{\rm bb}$ (km)	$19.4^{+0.1}_{-1.3}$	14.5 ± 0.1	$15.6^{+1.3}_{-0.1}$	$14.3^{+1.4}_{-0.1}$
Gauss	E (keV)	6.55 ± 0.16	$6.92^{+0.06}_{-0.08}$	$6.58^{+0.05}_{-0.17}$	$6.93^{+0.04}_{-0.06}$
...	σ (keV)	1.4 ± 0.3	$0.86^{+0.07}_{-0.05}$	1.48 ± 0.04	$1.24^{+0.05}_{-0.04}$
...	norm (10^{-2})	$9.5^{+0.2}_{-0.3}$	$1.96^{+0.17}_{-0.08}$	$7.8^{+0.2}_{-0.5}$	$4.0^{+0.1}_{-0.9}$
χ^2/d.o.f.[d]	...	113/112	142/118	117/111	169/121
$\rm Flux_{2-8\ keV}$ (10^{-9} erg s^{-1} cm^{-2})		4.95	5.50	4.26	5.14

Notes. Errors are reported at 68% CL.
[a] Fixed at 1.21 times the $N_{\rm H}$ value of warmabs.
[b] The Ni abundance was frozen at 5 to fit of an absorption feature at ∼7 keV; this value is in line with that reported by E. A. Saavedra et al. (2023).
[c] The inner radius for the diskbb component is estimated assuming an inclination at 70° (M. Diaz Trigo et al. 2012; R. D'Aì et al. 2014; E. A. Saavedra et al. 2023) and a distance of 7 kpc (R. M. Bandyopadhyay et al. 1999). For $R_{\rm bb}$ in the bbodyrad component, the same value for the distance was used.
[d] The higher χ^2 values at higher flux are probably related to an instrumental effect at low energy close to the Si edge at ∼1.84 keV.

displayed instead a continuous rotation in time (A. Bobrikova et al. 2024b).

A further time resolved analysis was performed by dividing the observation into six intervals, two during the dips and four outside of the dips. The polarimetric behavior with this time selection is reported in the right panel of Figure 5. It shows a rotation of PA from north to west, likely associated with an increase of PD during the dips. A similar behavior was observed during the dip in the first IXPE observation (A. Bobrikova et al. 2024b). Note that the second dip, which is shorter and less pronounced, has larger polarimetric uncertainties. Different time selections were attempted, but narrow selections result in a not-significant PD, while larger time selections report almost the same results, except when the selection starts to include periods with higher count rate.

We also performed the energy-resolved polarimetric analysis in each time interval of the right panel of Figure 5, but owing to the lower statistics no clear conclusion could be drawn. We note that Figure 5 of A. Bobrikova et al. (2024b) provided marginal evidence for polarimetric variability with energy across the dip of the first observation.

3.2. Spectral Analysis

During the third IXPE observation coordinated Swift-XRT and NICER observations were also available (see Section 2) and provided additional spectral coverage in the soft X-ray band. Therefore, we adopted the same spectral model introduced by M. Diaz Trigo et al. (2012) to model XMM-Newton data from GX 13+1. In the spectral and spectro-polarimetric analyses, we used XSPEC v.12.14.0 (K. A. Arnaud 1996). The continuum was modeled by the sum of a soft multicolor disk, i.e., diskbb (K. Mitsuda et al. 1984), describing the emission from the inner disk and/or the NS surface, and a harder Comptonized emission in an optically thick environment such as SL/BL, approximated here with bbodyrad. Absorption was modeled with TBabs, which is based on the abundances reported in J. Wilms et al. (2000). Our overall continuum model was thus tbabs*(diskbb+bbodyrad). The two Swift-XRT observations, which were both away from the dips, showed consistent spectra, with best-fit parameters also in agreement with those reported in Table 2 of A. Bobrikova et al. (2024a); see also Table 2.

The NICER data partially covered the IXPE observation with several snapshots, some of which were during dips (see Table 1 and Figure 1). To model the spectra in the dip and off-dip states, the data were selected on the basis of their hardness ratio (HR), as shown in Figure 1. By virtue of its better spectral capabilities and throughput (compared to IXPE and Swift-XRT), NICER resolved some of the absorption features reported in the literature (M. Diaz Trigo et al. 2012; R. D'Aì et al. 2014; E. A. Saavedra et al. 2023). In particular, residuals in the 6–8 keV region were clearly visible when the continuum model was fitted to the spectra. To account for those features, we followed the approach in M. Diaz Trigo et al. (2012) and included a warmabs component to model absorption by photoionized plasma along the line of sight. Moreover, a cabs component was included to account for the effects of Thomson/Compton scattering, which was found to be significant when modeling both the persistent and dipping emission (L. Boirin et al. 2005; M. Diaz Trigo et al. 2006, 2012). The latter component was forced to have ×1.21 the column density of the warmabs component (which accounts

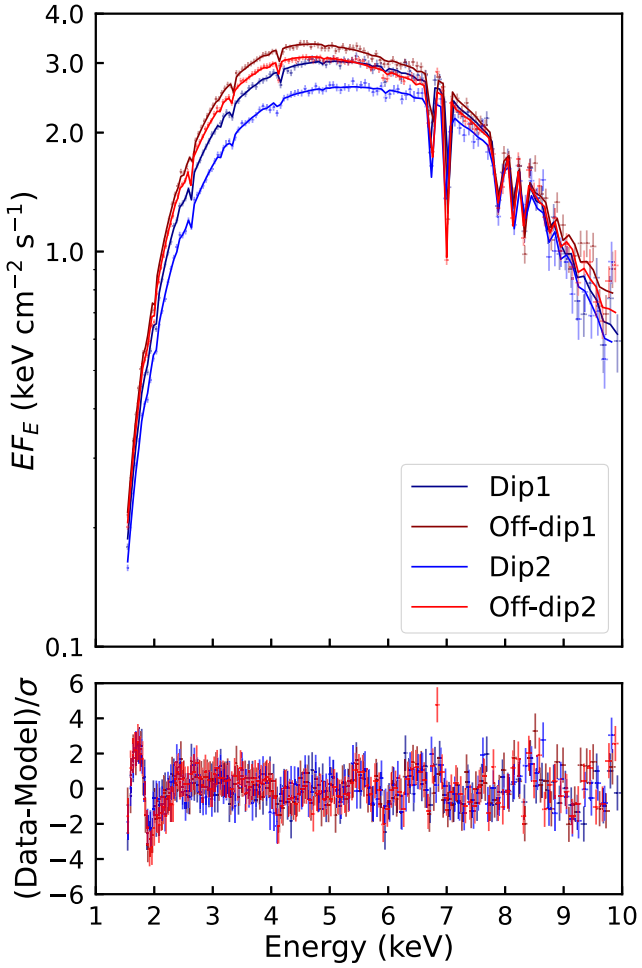

Figure 6. Best-fit spectral fits from NICER during dip and off-dip states in Observation IDs 77010102 and 77010103.

for the number of electrons per hydrogen atom for solar abundance material; B. Stelzer et al. 1999). Furthermore, a `Gaussian` component was included to account for a broad Fe line emission. The complete model we fit to the NICER spectra was thus `TBabs*warmabs*cabs*(diskbb+bbodyrad +Gauss)`. The best-fit results reported in Table 3 are in general agreement with those from XMM-Newton and Chandra observations (M. Diaz Trigo et al. 2012; R. D'Aì et al. 2014). The spectra are shown in Figure 6. Absorption was higher during the dips, especially during the first one, whereas the `diskbb` temperature was lower, ∼0.5 keV, than outside the dips (∼1 keV). The `bbodyrad` component remained instead at a nearly constant temperature of ∼1.1–1.2 keV.

3.3. Spectropolarimetric Analysis

In the spectropolarimetric analysis, we divided the IXPE data from the third observation into dip and off-dip states by using an intensity threshold of 28 cts s^{-1} (see the horizontal dashed–dotted line in the top panel of Figure 1). Owing to the lower throughput and spectral capabilities of IXPE (compared to those of NICER), our spectropolarimetric analysis resorted to a simplified model, `tbabs*(diskbb+bbodyrad+Gauss)`. The temperatures of both the `diskbb` and `bbodyrad` components, the energy and width of the Gaussian describing the iron line, were frozen at the values obtained from the NICER spectral fits.

Table 4
Best-fit Parameters for the Spectropolarimetric Model
`tbabs*(polconst*diskbb+polconst*bbodyrad+Gauss)`

	State	Dip	Off-dip
`tbabs`	$N_{\rm H}$ (10^{22} cm^{-2})	5.9 ± 0.3	4.40 ± 0.05
`diskbb`	$kT_{\rm in}$ (keV)	[0.5]	[1.0]
...	norm	5600 ± 600	241 ± 5
...	$R_{\rm in}^{a}$ (km)	90 ± 9	18.6 ± 0.4
`polconst1`	PD (%)	10 ± 4	< 4.3[b]
...	PA (deg)	64 ± 13	⋯
`bbodyrad`	$kT_{\rm bb}$ (keV)	[1.1]	[1.2]
...	norm	345 ± 2	223 ± 2
...	$R_{\rm bb}^{a}$ (km)	13.00 ± 0.08	10.5 ± 0.1
`polconst2`	PD (%)	5 ± 2	3.1 ± 1.1
...	PA (deg)	− 32 ± 7	− 8 ± 10
`Gauss`	E (keV)	[6.6]	[6.9]
...	σ (keV)	[1.4]	[1.0]
...	norm (10^{-2})	3.3 ± 0.2	2.1 ± 0.2
...	$f_{\rm DU1}$	[1]	[1]
...	$f_{\rm DU2}$	1.024 ± 0.005	1.021 ± 0.002
...	$f_{\rm DU3}$	1.000 ± 0.005	1.002 ± 0.002
χ^2/d.o.f.		433/431	465/431
Flux$_{2-8\ \rm keV}$ (10^{-9} erg s^{-1} cm^{-2})		3.7	4.8
Flux$_{\rm diskbb}$/Flux$_{\rm bbodyrad}$		0.2	0.5

Notes. The unabsorbed flux is 6.4×10^{-9} erg s^{-1} cm^{-2} in the 2–8 keV energy range, corresponding to a luminosity of 3.8×10^{37} erg s^{-1}. Errors are at 68% CL.
[a] The inner radius for the `diskbb` component was estimated assuming an inclination at 70° (M. Diaz Trigo et al. 2012; R. D'Aì et al. 2014; E. A. Saavedra et al. 2023) and a distance of 7 kpc (R. M. Bandyopadhyay et al. 1999). For $R_{\rm bb}$ in `bbodyrad` component and the unabsorbed luminosity, the same value of the distance was used.
[b] Upper limit at 90% CL.

As a first attempt, we assumed the same constant polarization for `diskbb+bbodyrad` and no polarization for the Gaussian (see, e.g., E. Churazov et al. 2002): `tbabs*(polconst*(diskbb+bbodyrad)+Gauss)`. The best-fit from the dip data gave[10] PD = 2.5% ± 0.7% and PA = −37° ± 8° (χ^2/d.o.f. = 441/433). For the off-dip data the best-fit yielded PD = 1.2% ± 0.3% with PA = −7° ± 7° (χ^2/d.o.f. = 469/433). These results parallel those obtained from the model-independent analysis: during the dips, when absorption was higher, the degree of polarization was higher, and the PA was different with respect to the off-dip state.

As a second step, we associated separate `polconst` polarization components to the `diskbb` and `bbodyrad` components: `tbabs*(polconst*diskbb+polconst*bbodyrad+Gauss)`. The best-fit results for this model are reported in Table 4. Polarization was detected at a level of PD ∼ 4% across the off-dip and dip states in the harder component (`bbodyrad`), together with marginal evidence for a PA change of ∼20°. For the `diskbb` component we found PD = 10% ± 4% in the dip state, whereas in the off-dip state we derived an upper limit of PD < 4.3% at 90% CL. We warn that the soft component's 10% PD during the dip should be considered with care, as the polarizations of the two components in the fit result are almost orthogonal,

[10] The other free parameters in the fit—such as the cross-normalizations, norm of `diskbb`, `bbodyrad`, and `Gaussian`—in both dip and off-dip cases have values compatible with the ones reported in Table 4.

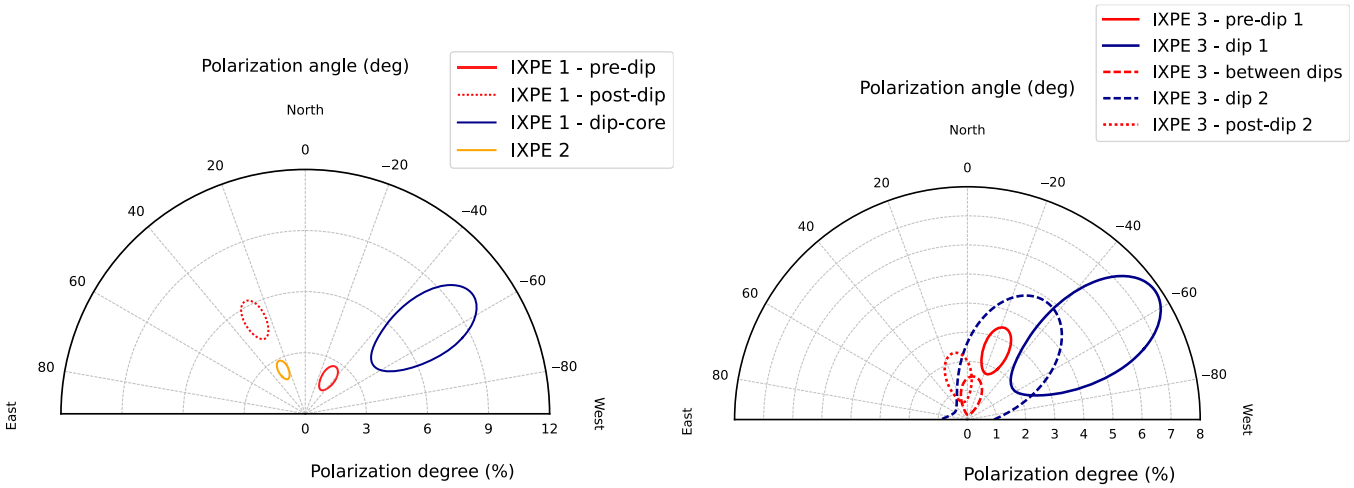

Figure 7. Comparison between the polarization in the first two IXPE observations of GX 13+1 (left) and this new one (right) to compare the polarization of the dips and of the source in off-dip states. Contours are at 90% CL.

meaning that they subtract from each other and partial degeneracy sets in.

4. Discussion

Polarization during the third IXPE observation of GX 13+1 showed marked variability. The behavior of the PA over time, shown in Figure 5, was complex and somewhat different from the continuous rotation seen during the first observation (A. Bobrikova et al. 2024b). Comparing this behavior with the trend of the hardness ratio reported in the bottom panels suggests that PD increased when HR was higher and that PA increased at higher count rates. The right panels of Figure 5 also show that the polarization parameters in the two dips are compatible with each other, to within the uncertainties.

In Figure 7, we compare the evolution of the polarization properties during the third and the previous two observations. It is seen that the PA in the two pre-dip intervals of the third observation was similar to that of the first observation's pre-dip. The PA during the two dips was compatible with the dip PA in the first observation. Then, after the second dip, the PA attained a value similar to the post-dip PA of the first observation, which in turn is compatible with the PA during the entire second IXPE observation (which did not show dips). We conclude that the polarimetric properties evolved in a similar manner across the three observations.

Concerning spectral properties, the HIDs in Figure 8 show a close similarity in shape and range during the three IXPE observations. Moreover, the simultaneous IXPE and Swift-XRT pointings of the off-dip state during the third and the second observations gave consistent best-fit parameters.

4.1. Comparison with Previous IXPE Observations and Combined Analysis

In consideration of the above similarities, we decided to combine the three IXPE observations in a single data set in order to search with higher sensitivity for correlated variability of PD and PA with intensity and HR. We first binned the HR data, in a manner similar to J. Rankin et al. (2024), and then selected the three HR intervals, almost equally spaced, shown in Figure 9.

In the higher HR interval, the one corresponding to the dips, we measured PD $\sim 4.3\%$ at PA $\sim -47°$, whereas the lower HR bin gave PD $\sim 2.4\%$ at PA $\sim 22°$. Thus, the total rotation was PA $\sim 70°$, a value similar to the continuous range spanned during the first IXPE observation of GX 13+1. The bin with intermediate HR displayed a lower PD ($\sim$1.3%) and a PA compatible with that of the low-HR bin. We also split this intermediate-HR bin into a low- and a high-intensity bin (see Figure 9), but no significant differences in their polarization properties were found.

A similar analysis was performed by dividing the combined data into four, almost equally spaced intensity bins, shown with different colors in Figure 10. In the lowest-intensity bin, we found PD $\sim 3\%$ at PA $\sim -40°$. For bins of progressively higher intensities, the polarization evolved as follows: PD $\sim 3.5\%$ at PA $\sim 32°$, PD $\sim 1.5\%$ at PA $\sim 11°$, and finally PD $\sim 1.5\%$ at $\sim -14°$ in the highest-intensity bin. Moreover, also in this case, the total variation of PA relative to the value in the dips was $\sim$70°.

Given the size of the uncertainty contours plotted in Figure 10, it can be concluded that these results are consistent with those reported in the HR binned analysis. In summary, low and low–intermediate intensity and high hardness were associated to a higher PD; higher intensity and lower hardness corresponded to a lower PD. The overall PA swing across the extremes was $\sim$70°.

4.2. Polarization and Spectral Components

These results may be interpreted as arising from variations of the continuum spectral components. We note that the harder Comptonized component (modeled with `bbodyrad`), which is believed to originate in the BL or the SL at the NS surface, contributed about half of the total flux in the off-dip state and about 80% during the dips. In fact, the softer component modeled with `diskbb` and associated with disk emission showed a more pronounced decrease in intensity during dips, leading to spectral hardening. In the NICER spectra we analyzed, the hardening appears to arise from the combination of a lower `diskbb` temperature and increased absorption (see Table 4).[11]

The polarization vectors of these two components, in systems with aligned BL/SL and disk symmetry axes, are expected to be $\sim$90° apart or parallel, depending on the geometry and optical depth of the BL/SL represented by the

[11] Such a spectral variation was also observed in the XMM-Newton data and could not be readily interpreted; see M. Diaz Trigo et al. (2012).

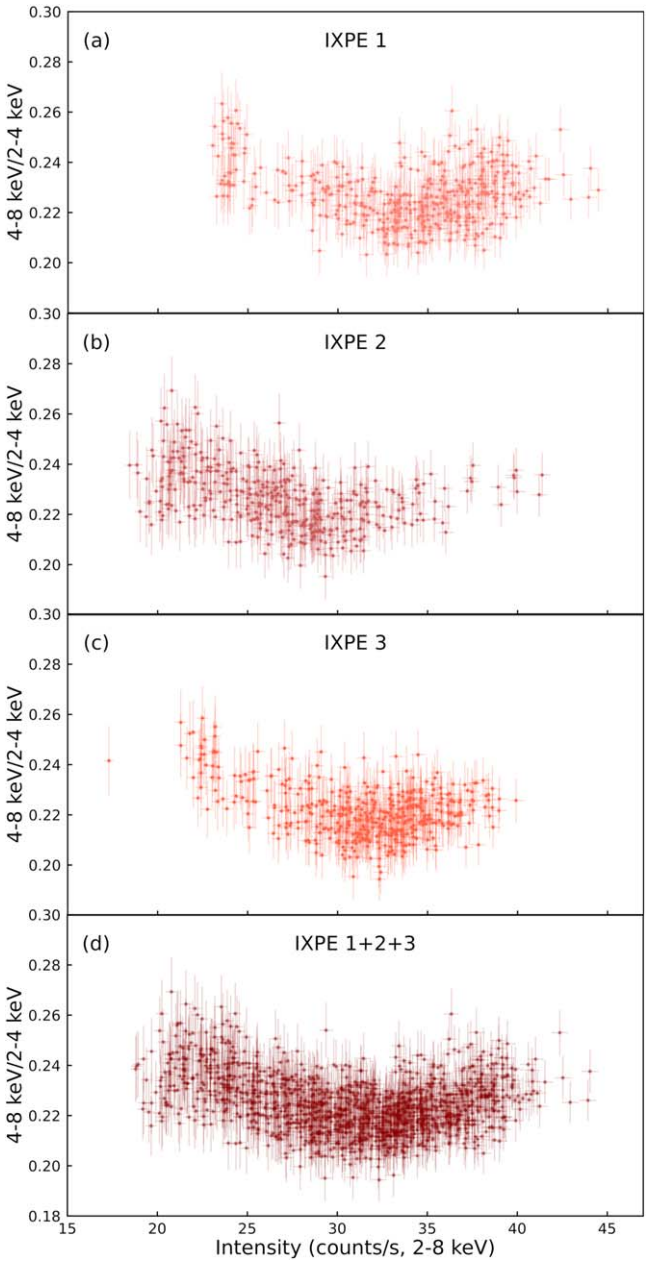

Figure 8. IXPE HID obtained for GX 13+1 from the different observations (panels (a)–(c)) and when the three observations are combined (d).

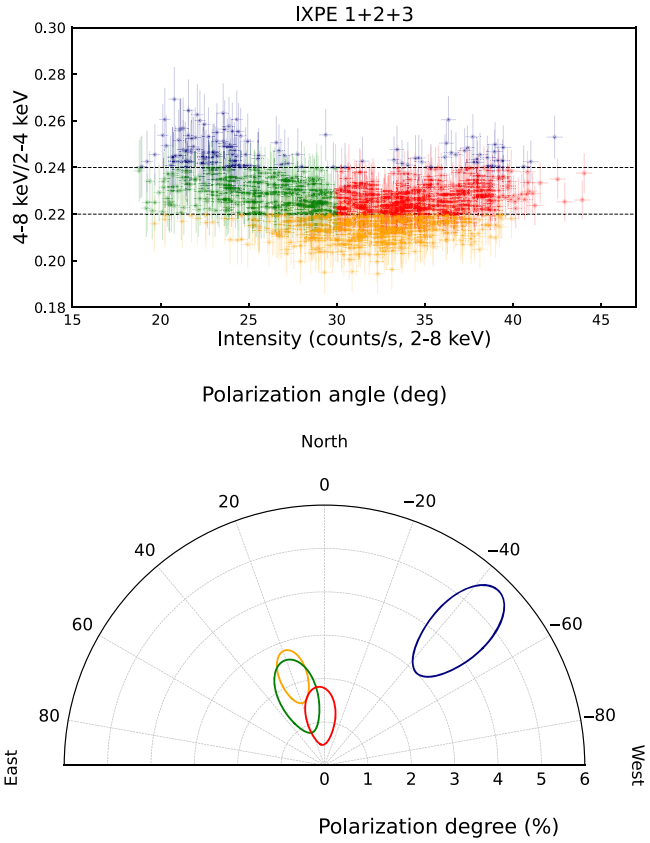

Figure 9. GX 13+1 HID from the three different IXPE observations where the different colors correspond to different HR and flux bins (top). The bottom panel reports the 90% CL polarization contours corresponding to the four different HR bins.

Comptonized spectrum (R. A. Sunyaev & L. G. Titarchuk 1985; V. Loktev et al. 2022; A. Bobrikova et al. 2024a). The mixing of these two components would generally produce a different polarization vector. In this case, variations of the two spectral components, giving rise to the intensity and hardness variations, would also translate into PD and PA variations from the sum of the two polarization vectors. In fact, for different HR values, the relative contribution of the two components changes and so does the resulting polarization vector. Intensity variations due to dips, which are associated with HR variations, can produce the same effect. This trend is visible, for example, in Figure 5 of A. Bobrikova et al. (2024a), where energy-resolved polarization shows a trend consistent with the spectral decomposition in terms of `diskbb` and `bbodyrad`: the polarization at higher energy was almost aligned with the hard component and in the softer energy bin with the polarization vector of the softer component.

Thus, during the dips the lower contribution of the soft component produces a hardening in the spectrum, and it is expected that the polarization will be dominated by the hard component. In our spectropolarimetric analysis, we found PD at $\sim$5% during the dip of the third observation. This value is higher than the maximum PD of 3%–4% expected for a source inclination of 60°–80°. For the soft `diskbb` component, a surprisingly high PD of 10% was obtained in the dip, which should be considered with care, whereas the value out of the dip was $<$4%. The latter limit is consistent with the maximum value of polarization expected for the disk component, which is 4% in the IXPE energy band (e.g., V. Loktev et al. 2022). Higher PD values are expected if a further polarized component is introduced in the model, such as a wind (see, e.g., A. P. Nitindala et al. 2024; R. Tomaru et al. 2024) or an ADC.

4.3. Dips and Polarization from ADC or Disk Wind

The shallow orbital modulation (see Figure 2 in this Letter and Figure 16 in R. Iaria et al. 2014) together with the presence of dips testifies that GX 13+1 is a high-inclination LMXB with an extended ADC and/or a disk wind, which scatters some photons from the X-ray-emitting regions along our line of sight. The shape of the folded light curve holds a clear resemblance to that of other LMXBs (see, e.g., A. N. Parmar & N. E. White 1988); its few-percent amplitude together with the luminosity close to the Eddington one demonstrates that the central X-ray source remains visible at all orbital phases. The periodic dips may coincide with superior conjunction of the NS, if material lost by the donor in its vicinity occults a fraction

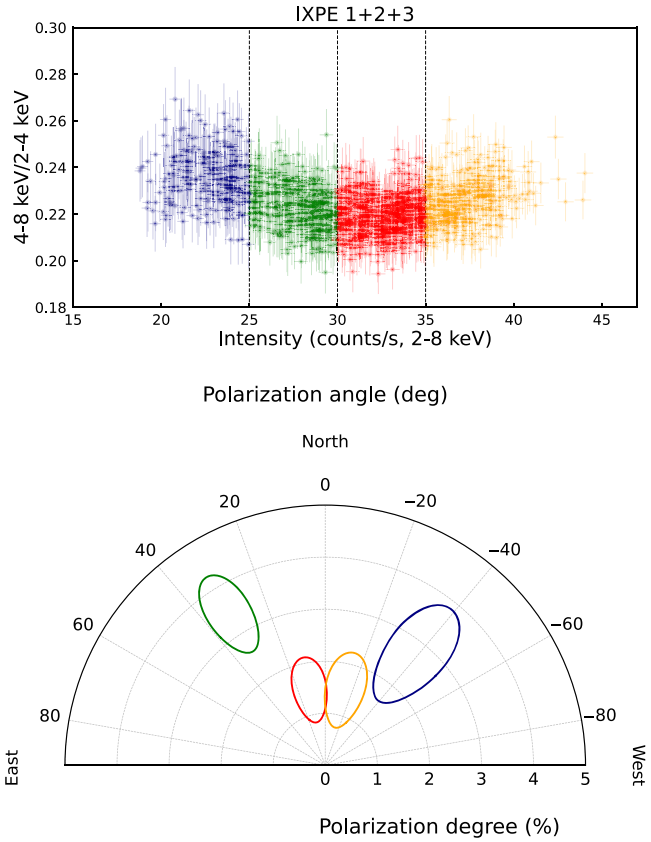

Figure 10. GX 13+1 HID from the three different IXPE observations where the different colors correspond to different bins in intensity (top). The bottom panel reports the polarization contours at 90% CL, corresponding to each intensity bin.

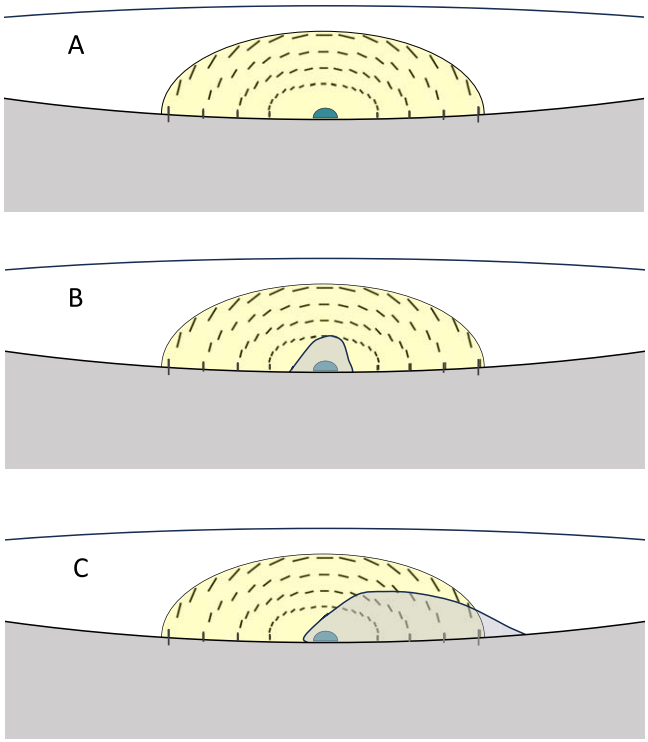

Figure 11. Sketch of the proposed geometry of GX 13+1 (not to scale). The gray region represents the outer disk rim, the yellow region the ADC, and the blue circle the central X-ray source. The black segments show the PA of the radiation scattered by the ADC. The PA at the observer (given by the average of the PAs) changes from the off-dip state (panel (A)) to the dip state, when a small clump obscures the central source and a negligible part of the ADC (panel (B)) and a large clump obscures the central source a fairly large fraction of the ADC (panel (C)).

of the X-ray radiation. The dips revealed by IXPE occurred at phases about −0.2 and 0.35 away from the periodic dips. Other LMXBs have displayed off-phase dips; for instance two dips per orbital cycle were observed occasionally in 4U 1916–053 (A. P. Smale et al. 1988). Dips separated by ∼0.5 in phase are believed to occur when clumps form close to the point where the accretion stream from the companion impacts the rim of the disk and about 180°away from that.

The characteristic size of the clumps, $R_{\rm clump}$, can be estimated from the dip duration, $T_{\rm dip}$, through the relation

$$R_{\rm clump} = \frac{T_{\rm dip}}{P_{\rm orb}} R_{\rm out}, \quad (1)$$

where $P_{\rm orb}$ is the orbital period and $R_{\rm out} \sim (1.0–2.6) \times 10^{12}$ cm is the disk outer radius (R. D'Aì et al. 2014). The clumps giving rise to the two dips of the third IXPE observation are estimated to be ∼(5–15) and (2–6) × 10^9 cm in size; that is, about 2 orders of magnitude smaller than the thickness of the disk, assuming that its half-height is 0.1–0.25 times $R_{\rm out}$. For the clumps to obscure the central X-ray source, the line of sight to GX 13+1 must almost graze the outer disk. An ADC size of $R_{\rm ADC} \sim 10^{10}$ cm was estimated in 4U 2129+470 (J. E. McClintock et al. 1982) and 4U 1822–37 (N. E. White & S. S. Holt 1982). GX 13+1, being a more luminous source, probably drives and photoionizes a larger corona: therefore, we assume $R_{\rm ADC} \sim 10^{10}$–10^{11} cm for it. Such a radius is about $\sim 10^3$ times larger than the regions where the bulk of the X-ray luminosity is produced. The photon source feeding the ADC can thus be considered point like, a condition under which the scattered radiation can possess a high PD, provided that the ADC is not spherically symmetric. For instance, a constant-density, oblate (ellipticity of ∼0.3), axially symmetric ADC fed by unpolarized photons would give rise to PD = 20% × τ (τ is the Thomson optical depth) when observed from a 60° inclination; see, e.g., Figure 4 in J. C. Brown & I. S. McLean (1977), where an ellipticity ∼0.3 corresponds to $\gamma \sim 0.24$.[12]

In the case of GX 13+1 (and likewise other LMXBs), the PD of the central X-ray source may thus be enhanced by scattering in an ADC if its optical depth is, say, of order ∼0.1. Besides increasing the PD to the observed level, the ADC may also cause a rotation of PA, together with an associated variation of the PD, when a clump giving rise to a dip passes in front of and obscures the central X-ray-emitting region while leaving the vision of the ADC virtually unaltered. In fact, by reducing the ratio of the (unscattered) photons reaching us directly from the central regions to those scattered along our line of sight by the ADC, the passage of the clumps will affect the mixing of the polarization vectors from the central region and the ADC leading to changes in the PA.[13] Some contribution to the rotation of the PA may also be produced when a large clump covers a significant fraction of the ADC, breaking the axial symmetry of the corona. These effects are illustrated in the sketch in panels (B) and (C) of Figure 11.

[12] γ is given by Equation (30) in J. C. Brown & I. S. McLean (1977) for $a = 3$.
[13] Except for the case in which the PAs of the central source and the ADC are coaligned.

Similar considerations would hold if the scattering region was the disk wind rather than the nonexpanding corona we outlined above (see also A. P. Nitindala et al. 2024). The warm absorber in the NICER spectral fits of GX 13+1 indicates column density of $\sim(5\text{–}6)\times10^{23}\,\mathrm{cm}^{-2}$ in the `cabs` component, corresponding to the Thomson optical depth of $\tau\sim0.3\text{–}0.4$. A fan-shaped, 30 degree aperture wind launched from a radius of 10^{10}–10^{11} cm, as inferred in M. Diaz Trigo et al. (2012), is similar in size and height to the ADC discussed above and may give rise to comparably large PDs.[14] Most of the optical depth of a wind with density scaling $\propto r^{-3}$ is reached within a few times the launching radius, such that the size of this equivalent "wind corona" of GX 13+1 exceeds the size of the clumps, and PA rotation can be produced in the same way as in the ADC case.

5. Conclusions

Based on the 2024 April IXPE observation of GX 13+1, together with coordinated observations from NICER and Swift-XRT, we studied the evolution of the spectral and polarization properties across the off-dip and dip states. Variations in PD and PA were detected that were correlated with the source intensity and hardness variations associated with the dips. The harder Comptonized component, likely arising from the BL/SL, and the softer blackbody-like emission from the disk had comparable fluxes in the off-dip intervals, when the PD was about 1%–2%. During the two dips, absorption by both neutral and warm gas increased, the Comptonized component became dominant, and the PD raised up to 4%–5%, displaying a $\sim70^\circ$ swing in PA. Joint analysis of the three IXPE observations led to a more precise polarimetric study, which provided confirmation of the relationship of the polarization with the source intensity and hardness and of the rotation of the PA.

Interpreting the high PD and the $\sim70^\circ$ PA variation in light of the polarization properties expected for disk and BL/SL emission proved difficult (see also A. Bobrikova et al. 2024a, 2024b). In fact, for systems whose components (the BL/SL and the disk) have symmetry axes aligned, polarization vectors are expected to be either parallel or orthogonal, with a PD lower than 4% for each of them (V. Loktev et al. 2022; R. A. Sunyaev & L. G. Titarchuk 1985). In this framework explaining PA rotation would require that the symmetry axis of the two components is offset and changing, for instance, through a misalignment between the disk and the NS axis, as suggested by A. Bobrikova et al. (2024b).

We propose that scattering in the ADC or in the disk wind, in association with obscuration by clumps causing the dips, can drive PA variations, as well as PD variations, in GX 13+1 as well as other LMXBs seen from high inclination. Detailed modeling would be required for this scenario, which also accounts for the energy distribution and polarization properties of the central emitting regions.

Acknowledgments

The Imaging X-ray Polarimetry Explorer (IXPE) is a joint US and Italian mission. The Italian contribution is supported by the Italian Space Agency (Agenzia Spaziale Italiana, ASI) through contract ASI-OHBI-2022-13-I.0, agreements ASI-INAF-2022-19-HH.0 and ASI-INFN-2017.13-H0, and its Space Science Data Center (SSDC) with agreements ASI-INAF-2022-14-HH.0 and ASI-INFN 2021-43-HH.0, and by the Istituto Nazionale di Astrofisica (INAF) and the Istituto Nazionale di Fisica Nucleare (INFN) in Italy. This research used data products provided by the IXPE Team (MSFC, SSDC, INAF, and INFN) and distributed with additional software tools by the High-Energy Astrophysics Science Archive Research Center (HEASARC) at NASA Goddard Space Flight Center (GSFC).

We thank Swift Project Scientists for approving our DDT request to observe GX 13+1. The authors acknowledge the NICER team for the simultaneous observations. A.D.M. and F.L.M. are partially supported by MAECI with grant CN24GR08 "GRBAXP: Guangxi-Rome Bilateral Agreement for X-ray Polarimetry in Astrophysics". This research has been supported by the Finnish Cultural Foundation grant 00240328 (A.B.) and the Academy of Finland grant 333112 (A.B., J.P.).

Facilities: IXPE, Swift, NICER.

Software: astropy (Astropy Collaborationf et al. 2013, 2018), SaoDS9, HEASoft (Nasa High Energy Astrophysics Science Archive Research Center Heasarc 2014), Stingray 2.0.0rc2 (D. Huppenkothen et al. 2019a, 2019b).

ORCID iDs

Alessandro Di Marco https://orcid.org/0000-0003-0331-3259
Fabio La Monaca https://orcid.org/0000-0001-8916-4156
Anna Bobrikova https://orcid.org/0009-0009-3183-9742
Luigi Stella https://orcid.org/0000-0002-0018-1687
Alessandro Papitto https://orcid.org/0000-0001-6289-7413
Juri Poutanen https://orcid.org/0000-0002-0983-0049
Maria Cristina Baglio https://orcid.org/0000-0003-1285-4057
Matteo Bachetti https://orcid.org/0000-0002-4576-9337
Vladislav Loktev https://orcid.org/0000-0001-6894-871X
Maura Pilia https://orcid.org/0000-0001-7397-8091
Daniele Rogantini https://orcid.org/0000-0002-5359-9497

References

Allen, J. L., Schulz, N. S., Homan, J., et al. 2018, ApJ, 861, 26
Arnaud, K. A. 1996, in ASP Conf. Ser., Vol. 101, Astronomical Data Analysis Software and Systems V, ed. G. H. Jacoby & J. Barnes (San Francisco, CA: ASP), 17
Astropy Collaboration, Price-Whelan, A. M., Sipőcz, B. M., et al. 2018, AJ, 156, 123
Astropy Collaboration, Robitaille, T. P., Tollerud, E. J., et al. 2013, A&A, 558, A33
Bachetti, M., Huppenkothen, D., Khan, U., et al. 2024, StingraySoftware/stingray: Release v2.1, Zenodo, doi:10.5281/zenodo.11383212
Baglio, M. C., DAvanzo, P., Campana, S., & Russell, D. M. 2017, Galax, 5, 62
Baldini, L., Bucciantini, N., Lalla, N., et al. 2022, SoftX, 19, 101194
Bandyopadhyay, R. M., Shahbaz, T., Charles, P. A., & Naylor, T. 1999, MNRAS, 306, 417
Bobrikova, A., Di Marco, A., La Monaca, F., et al. 2024a, A&A, 688, A217
Bobrikova, A., Forsblom, S. V., Di Marco, A., et al. 2024b, A&A, 688, A170
Boirin, L., Méndez, M., Dìaz Trigo, M., Parmar, A. N., & Kaastra, J. S. 2005, A&A, 436, 195
Brown, J. C., & McLean, I. S. 1977, A&A, 57, 141
Churazov, E., Sunyaev, R., & Sazonov, S. 2002, MNRAS, 330, 817
Cocchi, M., Gnarini, A., Fabiani, S., et al. 2023, A&A, 674, L10
Corbet, R. H. D., Pearlman, A. B., Buxton, M., & Levine, A. M. 2010, ApJ, 719, 979
Cottam, J., Sako, M., Kahn, S. M., Paerels, F., & Liedahl, D. A. 2001, ApJL, 557, L101
D'Aì, A., Iaria, R., Di Salvo, T., et al. 2014, A&A, 564, A62
Di Marco, A., Costa, E., Muleri, F., et al. 2022, AJ, 163, 170
Di Marco, A. & IXPE Science Team 2024, Astron. Nachr., e20240126

[14] However, it must be accounted for a factor $f<1$ resulting from the lower solid angle subtended by the wind at the central source; $f\sim0.5$ for this geometry.

Di Marco, A., La Monaca, F., Poutanen, J., et al. 2023a, ApJL, 953, L22
Di Marco, A., Soffitta, P., Costa, E., et al. 2023b, AJ, 165, 143
Dìaz Trigo, M., Parmar, A. N., Boirin, L., Méndez, M., & Kaastra, J. S. 2006, A&A, 445, 179
Dìaz Trigo, M., Sidoli, L., Boirin, L., & Parmar, A. N. 2012, A&A, 543, A50
Diaz Trigo, M., Sidoli, L., Parmar, A., & Boirin, L. 2009, in AIP Conf. Ser. 1248, X-ray Astronomy 2009; Present Status, Multi-Wavelength Approach and Future Perspectives, ed. A. Comastri, L. Angelini, & M. Cappi (Melville, NY: AIP), 153
Fabian, A. C., Rees, M. J., Stella, L., & White, N. E. 1989, MNRAS, 238, 729
Fabiani, S., Capitanio, F., Iaria, R., et al. 2024, A&A, 684, A137
Farinelli, R., Fabiani, S., Poutanen, J., et al. 2023, MNRAS, 519, 3681
Fleischman, J. R. 1985, A&A, 153, 106
Gehrels, N., Chincarini, G., Giommi, P., et al. 2004, ApJ, 611, 1005
Gendreau, K. C., Arzoumanian, Z., Adkins, P. W., et al. 2016, Proc. SPIE, 9905, 99051H
George, I. M., & Fabian, A. C. 1991, MNRAS, 249, 352
Giridharan, L., Thomas, N. T., Gudennavar, S. B., & Bubbly, S. G. 2023, MNRAS, 527, 11855
Hasinger, G., & van der Klis, M. 1989, A&A, 225, 79
Homan, J., van der Klis, M., Wijnands, R., Vaughan, B., & Kuulkers, E. 1998, ApJL, 499, L41
Huppenkothen, D., Bachetti, M., Stevens, A. L., et al. 2019a, ApJ, 881, 39
Huppenkothen, D., Bachetti, M., Stevens, A., et al. 2019b, JOSS, 4, 1393
Iaria, R., Di Salvo, T., Burderi, L., et al. 2014, A&A, 561, A99
Inogamov, N. A., & Sunyaev, R. A. 1999, AstL, 25, 269
Jimenez-Garate, M. A., Schulz, N. S., & Marshall, H. L. 2003, ApJ, 590, 432
Kallman, T. R., Angelini, L., Boroson, B., & Cottam, J. 2003, ApJ, 583, 861
La Monaca, F., Di Marco, A., Ludlam, R. M., et al. 2024, A&A, 691, A253
La Monaca, F., Di Marco, A., Poutanen, J., et al. 2024, ApJL, 960, L11
Loktev, V., Veledina, A., & Poutanen, J. 2022, A&A, 660, A25
Ludlam, R. M. 2024, Ap&SS, 369, 16
Maiolino, T., Laurent, P., Titarchuk, L., Orlandini, M., & Frontera, F. 2019, A&A, 625, A8
McClintock, J. E., London, R. A., Bond, H. E., & Grauer, A. D. 1982, ApJ, 258, 245
Miller, K. A., & Stone, J. M. 2000, ApJ, 534, 398
Mitsuda, K., Inoue, H., Koyama, K., et al. 1984, PASJ, 36, 741
Nasa High Energy Astrophysics Science Archive Research Center (Heasarc), 2014 HEAsoft: Unified Release of FTOOLS and XANADU, Astrophysics Source Code Library, ascl:1408.004
Nitindala, A. P., Veledina, A., & Poutanen, J. 2024, arXiv:2411.18299
Papitto, A., Torres, D. F., Rea, N., & Tauris, T. M. 2014, A&A, 566, A64
Parmar, A. N., & White, N. E. 1988, MmSAI, 59, 147
Popham, R., & Sunyaev, R. 2001, ApJ, 547, 355
Psaradaki, I., Costantini, E., Mehdipour, M., & Dìaz Trigo, M. 2018, A&A, 620, A129
Rankin, J., La Monaca, F., Di Marco, A., et al. 2024, ApJL, 961, L8
Romano, P., Campana, S., Chincarini, G., et al. 2006, A&A, 456, 917
Saade, M. L., Kaaret, P., Gnarini, A., et al. 2024, ApJ, 963, 133
Saavedra, E. A., Garcìa, F., Fogantini, F. A., et al. 2023, MNRAS, 522, 3367
Schnerr, R. S., Reerink, T., van der Klis, M., et al. 2003, A&A, 406, 221
Shakura, N. I., & Sunyaev, R. A. 1988, AdSpR, 8, 135
Smale, A. P., Mason, K. O., White, N. E., & Gottwald, M. 1988, MNRAS, 232, 647
Soffitta, P., Baldini, L., Bellazzini, R., et al. 2021, AJ, 162, 208
Stella, L., White, N. E., & Taylor, B. G. 1985, in Recent Results on Cataclysmic Variables. The Importance of IUE and Exosat Results on Cataclysmic Variables and Low-Mass X-Ray Binaries, ed. W. R. Burke (Paris: ESA), 125
Stelzer, B., Wilms, J., Staubert, R., Gruber, D., & Rothschild, R. 1999, A&A, 342, 736
Suleimanov, V., & Poutanen, J. 2006, MNRAS, 369, 2036
Sunyaev, R. A., & Titarchuk, L. G. 1985, A&A, 143, 374
Tomaru, R., Done, C., & Odaka, H. MNRAS 2024, 527, 7047
Ursini, F., Farinelli, R., Gnarini, A., et al. 2023, A&A, 676, A20
van der Klis, M. 1989, ARA&A, 27, 517
Weisskopf, M. C., Soffitta, P., Baldini, L., et al. 2022, JATIS, 8, 026002
White, N. E., & Holt, S. S. 1982, ApJ, 257, 318
White, T. R., Lightman, A. P., & Zdziarski, A. A. 1988, ApJ, 331, 939
Wilms, J., Allen, A., & McCray, R. 2000, ApJ, 542, 914